machines

MDPI

Article

Study on the Wear Performance of Spiroid Worm Drive with Steel–Steel Meshing

Yan Chen [1,*], Yun Pu [1] and Yonghong Chen [2]

[1] School of Artificial Intelligence, Chongqing Business Vocational College, No. 81 Daxuechengzhong Road, Shapingba, Chongqing 401331, China; puyun2009@163.com
[2] State Key Laboratory of Mechanical Transmission for Advanced Equipment, No. 174 Shazheng Road, Shapingba, Chongqing 400044, China; yh_chen@cqu.edu.cn
* Correspondence: chenyan-85@163.com; Tel.: +86-17783702800

Abstract: Worm drive belongs to the inclined plane transmission principle, and there is severe wear on the conjugate tooth surface. To reveal the wear mechanism and realize steel–steel meshing in the spiroid worm drive, the meshing performance model of conjugate tooth surface is established based on differential geometry theory and gear meshing principle, and the wear performance model is inferred by the Archard model and microscopic meshing performance. The wear performance of conjugate tooth surface is analyzed through the digital calculation, the pin-disk friction, and wear testing, as well as the spiroid worm drive prototype performance testing. The results show that there are good lubrication and anti-wear characteristics between the conjugate tooth surfaces, the wear amount on the right flank is twice that of the left flank, the wear depth at the loaded flank of the spiroid gear surface is smaller than that at the unloaded flank, as well as the feasibility of steel–steel meshing in worm drive has been confirmed.

Keywords: spiroid worm drive; meshing model; wear depth; dynamic experimental testing; steel–steel meshing

check for updates

Received: February 2025
Revised: 23 February 2025
Accepted: 25 February 2025
Published: 28 February 2025

Citation: Chen, Y.; Pu, Y.; Chen, Y. Study on the Wear Performance of Spiroid Worm Drive with Steel–Steel Meshing. *Machines* **2025**, *13*, 205. https://doi.org/10.3390/machines13030205

Copyright: © 2025 by the authors. Licensee MDPI, Basel, Switzerland. This article is an open access article distributed under the terms and conditions of the Creative Commons Attribution (CC BY) license (https://creativecommons.org/licenses/by/4.0/).

1. Introduction

Worm drive is a major form of mechanical transmission, which is characterized by wide transmission ratio range, compact structure, and low noise. In the motion transmission, it has a converging effect on the upstream errors of the transmission system, so it has been widely used in power transmission and has always been the preferred component for precision circular indexing mechanisms in machine tools and precision instruments. Due to the staggered shaft inclined plane transmission principle of the worm drive, there is a large relative sliding speed between the conjugate tooth surface of the worm drive. Therefore, the main forms of worm drive failure are severe wear and tooth surface adhesion. Reducing the wear performance of tooth surfaces, improving the lubrication performance of tooth surfaces, and enhancing the load-bearing capacity have always been a source of concern among the relevant scientific and technological circles, and various types of worm drive have been studied and proposed [1].

A spiroid worm drive is different from a traditional worm drive; the teeth of the spiroid gear are distributed on the end face and the material for the spiroid gear can be replaced with steel instead of bronze steel. Ease of manufacture and assembly due to face arrangement of spiroid gear teeth raises the possibility of easy adjustment of the lateral clearance in meshing [2–4].

In the field of spiroid worm drive meshing theory, Litvin and Fuentes developed methods for simulating meshing and contact of a spiroid worm drive [5], and introduced advanced stress analysis and meshing simulation of modified involute helical gears to improve gear performance and durability [6], as well as defined and modeled spherical involute and octoidal bevel gears to enhance the understanding of complex gear geometries [7], and these studies collectively improved the accuracy and efficiency of tooth contact analysis. Temirkhan proposed a computationally robust solution to the contact problem of two rotating gear surfaces in space, addressing critical challenges in gear contact analysis through advanced numerical techniques and significantly improving the stability and accuracy of gear meshing simulations [8]. Dudas created a unique geometric design for a spiroid worm drive featuring an axial arc profile, and the three-dimensional model of this drive pair was developed along with the production tool; a physical prototype was also fabricated using rapid prototyping technology [9]. Balajti contributed a new methodology for identifying and preventing undercutting positions by analyzing worm drives with a circular arc profile, and this approach defines the conditions under which the common normal aligns with the tangent plane at meshing points [10]. Zhao introduced a novel spiroid worm drive and proposed a reference point to determine the meshing line, and this theory also demonstrated the superior microscopic meshing characteristics of the new drive [11–15]. Li developed a two-dimensional generating surface method that shifts contact in spiroid worm drives from lines to points, and this method's effectiveness in achieving high performance and low noise was validated through numerical simulations and prototype testing [16]. Chen explored the evolution of meshing performance in spiroid worm drives with varying worm cone angles, and it analyzed induced normal curvature and lubrication angles and confirmed the viability of substituting a cylindrical worm for a spiroid worm through both simulations and prototype tests [17]. These studies collectively highlight the extensive and detailed nature of spiroid worm drive meshing theory, which significantly contributes to the optimal design of such drives.

In the field of spiroid worm drive manufacturing, Staniek introduced a technique for machining the spiroid gear though a linear cutting tool, and this method employs continuous indexing on the general CNC machine tools, complemented by an NC rotary table [18,19]. Tkachuk developed an approach involving cutter heads for spiroid gear manufacturing, and it includes detailed multi-tooth assembled tool design techniques for effective cutting [20]. Yang developed an innovative method to create the surface of worm gear hobs though the paraboloid surface [21]. Balajti addressed the issue of pitch errors on spiroid worm tooth surfaces caused by angular velocity fluctuations by designing a constant pitch drive pin [22]. Tkachuk also contributed a method to calculate the tool profiles of disk abrasive, enabling the profiling of disk abrasive for various spiroid worm tooth surfaces, and this methodology ensures high precision in processing the tooth surfaces of hardened grinding spiroid worms [23]. Chodola introduced a novel method for measuring the oil temperature in spiroid worm drives and designed an innovative test bench for this purpose [24]. Collectively, these advancements demonstrate that precision machining and testing technologies for spiroid worm and gear tooth surfaces have been effectively mastered.

The friction and wear properties of tooth surfaces play a crucial role in the failure of spiroid worm drives, which operate on the principle of inclined transmission. Tošić investigated the EHL occurring between the surface of worm drive with nonconjugate meshing, identifying and analyzing the geometric and kinematic design factors that affect the formation of elastohydrodynamic lubrication films in worm drives [25]. Mazurkow presented the elastohydrodynamic oil film properties of the spiroid worm drive, with the unknown quantity being the rotational speed of spiroid worm, and it can help designers

improve the durability and reliability of the spiroid worm drive [26]. Zaitsev presented a method for predicting spiroid worm drive by wear; the variability of loads and the number of cycles on the contact endurance and endurance are considered, and the wear of spiroid worm drive with steel 45 and bronze BrA9ZH4 are carried out [27]. Zengeya investigated the effects of cooling rates during injection molding on HDPE gears, demonstrating how mold temperature influences wear resistance and gear performance [28]. Aleksandar explored the impact of worm gear materials and lubricants on efficiency and friction coefficients, highlighting the critical role of material–lubricant interactions in optimizing gear performance [29]. The aforementioned research preliminarily explored the lubrication and wear performance of spiroid worm drives, but it has not yet been fully understood the operation characteristics of spiroid worm drive with steel–steel meshing.

This study focuses on the wear performance of spiroid worm drives with steel–steel meshing, establishing a detailed meshing performance model for tooth surfaces and infers a wear performance model based on the Archard model and microscopic meshing analysis. This approach enables a more accurate prediction of wear behavior under realistic operating conditions. Furthermore, this study validates the proposed models through a combination of digital calculations, pin-disk friction and wear testing, and spiroid worm drive prototype performance testing, providing a robust experimental foundation for the findings. The results confirm the feasibility of steel–steel meshing in spiroid worm drives, offering a significant advancement in the design and application of high-performance gear systems.

2. Mathematical Model of Spiroid Worm Drive

2.1. Tooth Surface of Spiroid Worm

The tooth surface on both sides of a spiroid worm are generated by a turning tool with conical helix, as shown in Figures 1 and 2 [30].

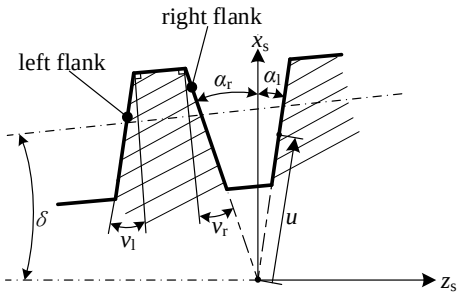

Figure 1. Tooth profile of a spiroid worm.

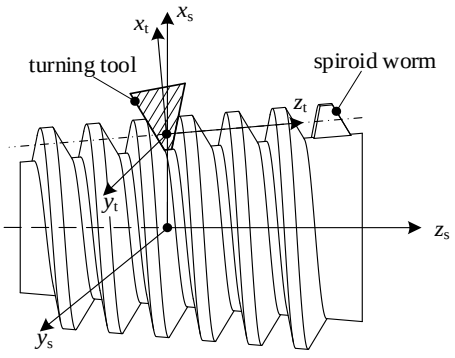

Figure 2. Forming principle of spiroid worm.

In Figure 1, u denotes the radial parameter of tooth surface, and δ represents the cone angle of a spiroid worm. α_l labels the pressure angle of the left flank, while α_r labels the pressure angle of the right flank. v_l represents the tooth profile angles of the left flank, while

v_r represents the tooth profile angles of the right flank. In Figure 2, the S_s (O_s: x_s, y_s, z_s) and S_t (O_t: x_t, y_t, z_t) are fixed to the spiroid worm and turning tool, respectively.

The mathematical model of the spiroid worm left flank and right flank can be written as follows:

$$\begin{cases} \boldsymbol{r}_l^{(s)} = r_{lx} i_s + r_{ly} j_s + r_{lz} k_s \\ r_{lx} = (u\cos\alpha_l + p_l\varphi_u \tan\delta)\cos\varphi_u \\ r_{ly} = (u\cos\alpha_l + p_l\varphi_u \tan\delta)\sin\varphi_u \\ r_{lz} = p_l\varphi_u + u\sin\alpha_l \end{cases} \tag{1}$$

$$\begin{cases} r_r^{(s)} = r_{rx} i_s + r_{ry} j_s + r_{rz} k_s \\ r_{rx} = (u\cos\alpha_r + p_r\varphi_u \tan\delta)\cos\varphi_u \\ r_{ry} = (u\cos\alpha_r + p_r\varphi_u \tan\delta)\sin\varphi_u \\ r_{rz} = p_r\varphi_u - u\sin\alpha_r \end{cases} \tag{2}$$

where $r_l^{(s)}$ express the tooth surface equations of the left flank, while $r_r^{(s)}$ express the tooth surface equations of the right flank. φ_u represents the angular displacement of the spiroid worm, while p_t denotes the radial screw parameter of tooth surface.

Based on the differential geometry and meshing theory [30], the unit normal vector of the spiroid worm tooth surface can be denoted as follows:

$$\begin{cases} \boldsymbol{n}_l^{(s)} = n_{lx} i_s + n_{ly} j_s + n_{lz} k_s \\ n_{lx} = \sin\alpha_l[\cos\varphi_u(u\cos\alpha_l + \varphi_u p_l \tan\delta) + p_l \tan\delta \sin\varphi_u] + p_l\cos\alpha_l \sin\varphi_u \\ n_{ly} = \sin\alpha_l[\sin\varphi_u(u\cos\alpha_l + \varphi_u p_l \tan\delta) - p_l \tan\delta \cos\varphi_u] - p_l\cos\alpha_l \cos\varphi_u \\ n_{lz} = \cos\alpha_l(\varphi_u p_l \tan\delta + u\cos\alpha_l) \end{cases} \tag{3}$$

$$\begin{cases} \boldsymbol{n}_r^{(s)} = n_{rx} \boldsymbol{i}_s + n_{ry} \boldsymbol{j}_s + n_{rz} \boldsymbol{k}_s \\ n_{rx} = -\sin\alpha_r[\cos\varphi_u(u\cos\alpha_r + \varphi_u p_r \tan\delta) + p_r \tan\delta \sin\varphi_u] + p_r\cos\alpha_r \sin\varphi_u \\ n_{ry} = -\sin\alpha_r[\sin\varphi_u(u\cos\alpha_r + \varphi_u p_r \tan\delta) - p_r \tan\delta \cos\varphi_u] - p_r\cos\alpha_r \cos\varphi_u \\ n_{rz} = \cos\alpha_r(\varphi_u p_r \tan\delta + u\cos\alpha_r) \end{cases} \tag{4}$$

2.2. Meshing of Spiroid Worm Drive

During the enveloping process and meshing state of the spiroid worm drive, the spiroid worm is positioned on the end-face of the spiroid gear with a specific offset distance, as illustrated in Figure 3.

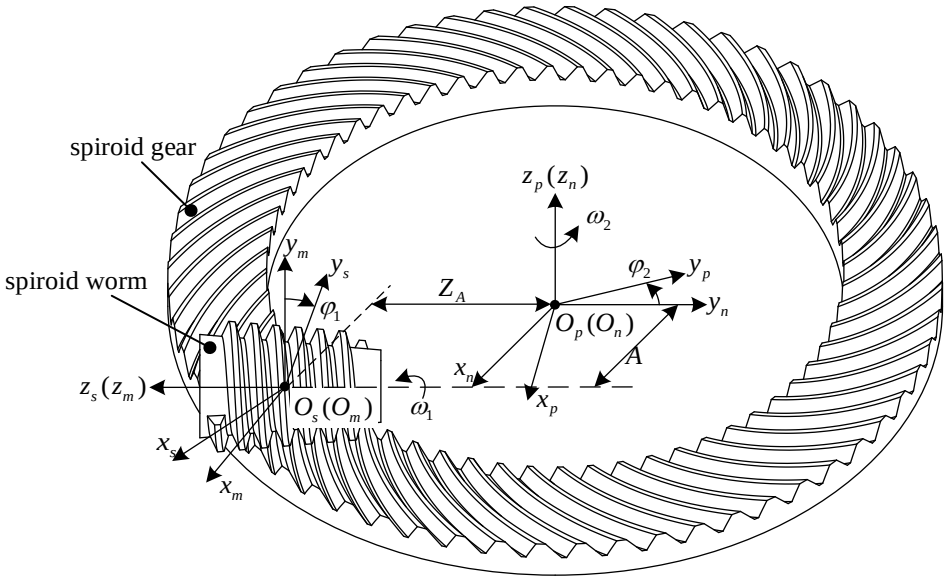

Figure 3. Enveloping process of a spiroid worm drive.

The initial orientation of the spiroid worm is defined by the space-fixed coordinate system $S_m(O_m: x_m, y_m, z_m)$ grounded at a reference point, while the spiroid gear is defined by $S_n(O_n: x_n, y_n, z_n)$. The spiroid worm revolves around its z_s axis with the angular velocity vector of ω_1, while the spiroid gear revolves around its z_p axis with the angular velocity vector of ω_2. Meanwhile, $S_s(O_s: x_s, y_s, z_s)$ and $S_p(O_p: x_p, y_p, z_p)$ are the moving coordinate systems; $S_s(O_s: x_s, y_s, z_s)$ is rigidly attached to the spiroid worm, while $S_p(O_p: x_p, y_p, z_p)$ is firmly connected to the spiroid gear. The instantaneous angular displacement of the worm and gear are denoted as φ_1 and φ_2, respectively. Furthermore, the spiroid worm has an installation offset distance of Z_A, and the center distance is A, while the transmission ratio is given as $i_{12} = \omega_1/\omega_2 = \varphi_1/\varphi_2$.

The relative velocity of instantaneous meshing point on the tooth surface can be derivated as:

$$\begin{cases} \boldsymbol{v}^{(sp)} = \boldsymbol{\omega}_1{}^{(s)} \times \boldsymbol{r}^{(s)} - \boldsymbol{\omega}_2{}^{(p)} \times \boldsymbol{r}^{(p)} \\ \quad = \boldsymbol{\omega}^{(sp)} \times \boldsymbol{r}^{(s)} - \boldsymbol{\omega}_2{}^{(p)} \times \boldsymbol{o}_1\boldsymbol{o}_2 \\ \boldsymbol{\omega}_1{}^{(s)} = w_1\boldsymbol{k}_s \\ \boldsymbol{\omega}_2{}^{(p)} = w_2\boldsymbol{k}_p = w_2(\sin\varphi_1\boldsymbol{i}_s + \cos\varphi_1\boldsymbol{j}_s) \\ \boldsymbol{\omega}^{(sp)} = -w_2\sin\varphi_1\boldsymbol{i}_s - w_2\cos\varphi_1\boldsymbol{j}_s + w_1\boldsymbol{k}_s \\ \boldsymbol{o}_1\boldsymbol{o}_2 = A\cos\varphi_1\boldsymbol{i}_s - A\sin\varphi_1\boldsymbol{j}_s + Z_A\boldsymbol{k}_s \end{cases} \tag{5}$$

To streamline the computational procedure, $\omega_1 = 1$ is taken and the relative motion velocity can be simplified as follows:

$$\begin{cases} \boldsymbol{v}_l^{(sp)} = \boldsymbol{v}_{lx}{}^{(sp)}\boldsymbol{i}_s + \boldsymbol{v}_{ly}{}^{(sp)}\boldsymbol{j}_s + \boldsymbol{v}_{lz}{}^{(sp)}\boldsymbol{k}_s \\ v_{lx}{}^{(sp)} = -r_{ly} - i_{12}r_{lz}\cos\varphi_1 - Z_A i_{12}\cos\varphi_1 \\ v_{ly}{}^{(sp)} = r_{lx} + i_{12}r_{lz}\sin\varphi_1 + Z_A i_{12}\sin\varphi_1 \\ v_{lz}{}^{(sp)} = i_{12}r_{ly}\cos\varphi_1 - i_{12}r_{ly}\sin\varphi_1 + Ai_{12} \end{cases} \tag{6}$$

$$\begin{cases} \boldsymbol{v}_r^{(sp)} = v_{rx}{}^{(sp)}\boldsymbol{i}_s + v_{ry}{}^{(sp)}\boldsymbol{j}_s + v_{rz}{}^{(sp)}\boldsymbol{k}_s \\ v_{rx}{}^{(sp)} = -r_{ry} - i_{12}r_{rz}\cos\varphi_1 - Z_A i_{12}\cos\varphi_1 \\ v_{ry}{}^{(sp)} = r_{rx} + i_{12}r_{rz}\sin\varphi_1 + Z_A i_{12}\sin\varphi_1 \\ v_{rz}{}^{(sp)} = i_{12}r_{rx}\cos\varphi_1 - i_{12}r_{ry}\sin\varphi_1 + Ai_{12} \end{cases} \tag{7}$$

According to the gear geometry and applied theory [30], the spiroid worm drive tooth surface should meet the following equations:

$$\boldsymbol{\Phi}_l = \boldsymbol{n}_l^{(s)} \bullet \boldsymbol{v}_l^{(sp)} = 0 \tag{8}$$

$$\boldsymbol{\Phi}_r = \boldsymbol{n}_r^{(s)} \bullet \boldsymbol{v}_r^{(sp)} = 0 \tag{9}$$

Substituting Equations (3) and (6) into Equation (8), the meshing equation of the spiroid worm left flank can be obtained, while substituting Equations (4) and (7) into Equation (9) to obtain the meshing equation of the spiroid worm tooth right flank.

2.3. Tooth Surface of Spiroid Gear

The tooth profile of a spiroid gear is generated by the enveloping action of a spiroid worm tooth surface. This profile can be mathematically derived by integrating Equations (1) and (2) with Equations (8) and (9), followed by applying the transformation matrix of coordinates from S_s to S_p.

The left flank of spiroid gear can be described as follows:

$$\begin{cases} \boldsymbol{r}_{\mathrm{l}}^{(\mathrm{p})} = r_{\mathrm{l}x}^{(\mathrm{p})}\boldsymbol{i}_{\mathrm{p}} + r_{\mathrm{l}y}^{(\mathrm{p})}\boldsymbol{j}_{\mathrm{p}} + r_{\mathrm{l}z}^{(\mathrm{p})}\boldsymbol{k}_{\mathrm{p}} \\ r_{\mathrm{l}x}^{(\mathrm{p})} = r_{\mathrm{l}x}\cos\varphi_1\cos\varphi_2 - r_{\mathrm{l}y}\sin\varphi_1\cos\varphi_2 + r_{\mathrm{l}z}\cos\varphi_2 + A\cos\varphi_2 - Z_A\sin\varphi_2 \\ r_{\mathrm{l}y}^{(\mathrm{p})} = -r_{\mathrm{l}x}\cos\varphi_1 sin\varphi_2 + r_{\mathrm{l}y}\sin\varphi_1\sin\varphi_2 - r_{\mathrm{l}z}\cos\varphi_2 - A\sin\varphi_2 - Z_A\cos\varphi_2 \\ r_{\mathrm{l}z}^{(\mathrm{p})} = r_{\mathrm{l}x}\sin\varphi_1 - r_{\mathrm{l}y}\cos\varphi_1 \\ r_{\mathrm{l}x} = (u\cos\alpha_1 + p_1\varphi_u\tan\delta)\cos\varphi_u \\ r_{\mathrm{l}y} = (u\cos\alpha_1 + p_1\varphi_u\tan\delta)\sin\varphi_u \\ r_{\mathrm{l}z} = p_1\varphi_u + u\sin\alpha_1 \\ \boldsymbol{\Phi}_{\mathrm{l}} = 0 \end{cases} \tag{10}$$

The right flank of spiroid gear can be described as follows:

$$\begin{cases} \boldsymbol{r}_{\mathrm{r}}^{(\mathrm{p})} = r_{\mathrm{r}x}^{(\mathrm{p})}\boldsymbol{i}_{\mathrm{p}} + r_{\mathrm{r}y}^{(\mathrm{p})}\boldsymbol{j}_{\mathrm{p}} + r_{\mathrm{r}z}^{(\mathrm{p})}\boldsymbol{k}_{\mathrm{p}} \\ r_{\mathrm{r}x}^{(\mathrm{p})} = r_{\mathrm{r}x}\cos\varphi_1\cos\varphi_2 - r_{\mathrm{r}y}\sin\varphi_1\cos\varphi_2 + r_{\mathrm{r}z}\cos\varphi_2 + A\cos\varphi_2 - Z_A\sin\varphi_2 \\ r_{\mathrm{r}y}^{(\mathrm{p})} = -r_{\mathrm{r}x}\cos\varphi_1 sin\varphi_2 + r_{\mathrm{r}y}\sin\varphi_1\sin\varphi_2 - r_{\mathrm{r}z}\cos\varphi_2 - A\sin\varphi_2 - Z_A\cos\varphi_2 \\ r_{\mathrm{r}z}^{(\mathrm{p})} = r_{\mathrm{r}x}\sin\varphi_1 - r_{\mathrm{r}y}\cos\varphi_1 \\ r_{\mathrm{r}x} = (u\cos\alpha_{\mathrm{r}} + p_{\mathrm{r}}\varphi_u\tan\delta)\cos\varphi_u \\ r_{\mathrm{r}y} = (u\cos\alpha_{\mathrm{r}} + p_{\mathrm{r}}\varphi_u\tan\delta)\sin\varphi_u \\ r_{\mathrm{r}z} = p_{\mathrm{r}}\varphi_u - u\sin\alpha_{\mathrm{r}} \\ \boldsymbol{\Phi}_{\mathrm{r}} = 0 \end{cases} \tag{11}$$

2.4. Meshing Performance of Spiroid Worm Drive

The induced normal curvature represents the microscopic touching relationship between two meshing tooth surfaces at their contact point, serving as a key indicator for assessing tooth surface wear in spiroid worm drives. Generally, a lower induced curvature value correlates with improved wear resistance. To calculate this parameter at the contact point within the meshing zone, the following equation can be applied [17]:

$$\begin{cases} K_\sigma = \dfrac{\frac{1}{D^4}\left[\boldsymbol{\Phi_u}(F\frac{\partial \boldsymbol{r}^{(\mathrm{s})}}{\partial\varphi_u} - G\frac{\partial \boldsymbol{r}^{(\mathrm{s})}}{\partial u}) - \boldsymbol{\Phi_{\varphi u}}(E\frac{\partial \boldsymbol{r}^{(\mathrm{s})}}{\partial\varphi_u} - F\frac{\partial \boldsymbol{r}^{(\mathrm{s})}}{\partial u})\right]^2}{\boldsymbol{a}\cdot\boldsymbol{v}^{(12)} + w_1w_2[n_{\mathrm{x}}(r_z+A)\sin\varphi_1 + n_y(r_z+A)\cos\varphi_1 - n_{iz}(r_x\sin\varphi_1 + r_y\cos\varphi_1)]} \\ \boldsymbol{\Phi_u} = \frac{\partial \boldsymbol{\Phi}}{\partial u}\ \boldsymbol{\Phi_{\varphi u}} = \frac{\partial \boldsymbol{\Phi}}{\partial\varphi_u} \\ E = \left(\frac{\partial \boldsymbol{r}^{(\mathrm{s})}}{\partial u}\right)^2\ G = \left(\frac{\partial \boldsymbol{r}^{(\mathrm{s})}}{\partial\varphi_u}\right)^2 \\ F = \frac{\partial \boldsymbol{r}^{(\mathrm{s})}}{\partial u}\cdot\frac{\partial \boldsymbol{r}^{(\mathrm{s})}}{\partial\varphi_u}\ D^2 = EG - F^2 \\ \boldsymbol{a} = \frac{1}{D^2}\left[\boldsymbol{\Phi_u}(F\frac{\partial \boldsymbol{r}^{(\mathrm{s})}}{\partial\varphi_u} - G\frac{\partial \boldsymbol{r}^{(\mathrm{s})}}{\partial u}) - \boldsymbol{\Phi_{\varphi u}}(E\frac{\partial \boldsymbol{r}^{(\mathrm{s})}}{\partial\varphi_u} - F\frac{\partial \boldsymbol{r}^{(\mathrm{s})}}{\partial u})\right] \end{cases} \tag{12}$$

The lubrication angle is defined as the angle formed between the contact line and the relative velocity vector at any moment, serving as a critical factor in assessing tooth surface wear in spiroid worm drives. A greater lubrication angle generally enhances the development of a hydrodynamic oil film as well as the tooth surface wear resistance. To calculate this angle at the contact point within the meshing zone, the following equation can be utilized [17]:

$$\theta_v = \arcsin\left(\frac{\boldsymbol{a}_x v_x^{(12)} + \boldsymbol{a}_y v_y^{(12)} + \boldsymbol{a}_z v_{\mathrm{z}}^{(12)}}{\sqrt{\boldsymbol{a}_x{}^2 + \boldsymbol{a}_y{}^2 + \boldsymbol{a}_z{}^2}\cdot\sqrt{\left(v_x^{(12)}\right)^2 + \left(v_y^{(12)}\right)^2 + \left(v_y^{(12)}\right)^2}}\right) \tag{13}$$

3. Wear Performance of Spiroid Worm Drive

3.1. Numerical Analysis of Meshing Performance

To evaluate the meshing performance, the key design parameters are shown in Table 1.

Table 1. Key design parameters of spiroid worm drive.

Parameters	Unit	Value
Central distance	A/mm	94
Gear Ratio	i_{12}	50
Modulu along generatrix of worm	m_δ/mm	3.73
Number of worm threads	Z_1	1
Thread direction of worm		Right
Helix parameter	p/mm	1.8579
Diameter coefficient for worm	q	14
Cone angle of worm	$\delta/^\circ$	5
Pressure angle of left flank	$\alpha_1/\circ$	10
Pressure angle of right flank	$\alpha_e/\circ$	30
The full tooth height of worm	h_a/mm	8.3925
The working tooth height of worm	h_w/mm	7.46
Pinion mounting distance	Z_A/mm	65
Calculated length of worm thread	L_w/mm	68.62
Half cone angle of worm gear	$\delta_{a2}/\circ$	83

Based on Equation (12), the induced normal curvature k_δ on the spiroid gear tooth surface can be calculated, and on the results for the left flank and right flank are shown in Figure 4. It can be known that the induced normal curvature is between 0.032 mm^{-1} and 0.039 mm^{-1} on the left flank of the spiroid gear, while it is 0.016 mm^{-1} and 0.032 mm^{-1} on the right flank. Additionally, the induced normal curvature at the tooth tip is less pronounced compared to that at the tooth root. The contact stress at the tooth tip is smaller, with superior wear and abrasion resistance.

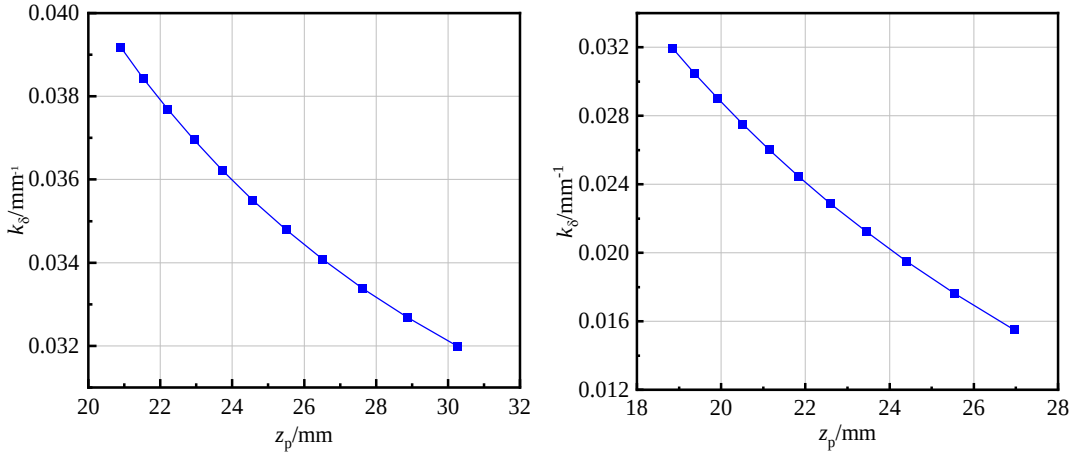

(**a**) Left flank (**b**) Right flank

Figure 4. The k_δ on spiroid gear tooth surface.

Based on Equation (13), the lubrication angle θ_v on the spiroid gear tooth surface can be calculated, and the results for the left flank and right flank are shown in Figure 5. It can be known that the lubrication angle is between 74° and 80° on the left flank of the spiroid gear, while it is 76° and 88° on the right flank, and the lubrication angle on the tooth tip is bigger than that on the tooth root. The lubrication effect on the tooth tip is better, resulting in superior wear and abrasion resistance.

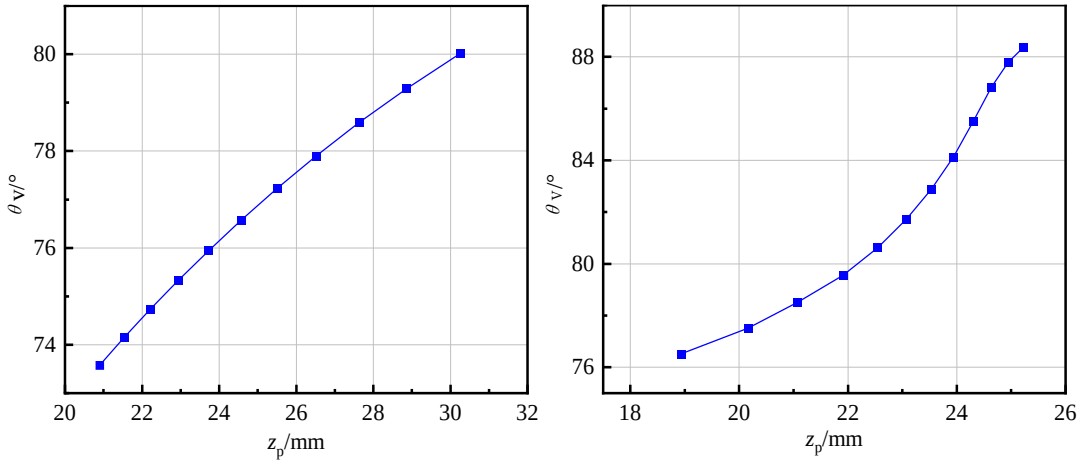

(**a**) Left flank (**b**) Right flank

Figure 5. The θ_v on a spiroid gear tooth surface.

3.2. Mathematical Model of Wear Performance

Based on the Archard model [31], it can be expressed as follows:

$$\frac{V}{s} = K\frac{F_n}{H} \tag{14}$$

where V represents the wear volume, while K is the wear coefficient which depends on the material properties. s denotes the sliding distance of two surfaces, and H signifies the hardness of the contact surface material, while F_n stands for the normal load.

By incorporating the tooth surface wear and considering the contact area, it can be modified as follows:

$$\frac{h}{s} = kp \tag{15}$$

where h represents the wear depth, which is the ratio of wear volume to contact area. k represents the wear coefficient, which is the ratio of K to H. p signifies the contact pressure.

The wear coefficient k serves as an indicator of a material's wear resistance, with its value influenced by factors such as lubrication conditions, material properties, and operational parameters. It can be expressed as follows:

$$k = \frac{3.981 \times 10^{29}}{E_\Sigma}(\alpha_0 E_\Sigma)^{-7.377}\left(\frac{f_n}{E_\Sigma \rho_\Sigma}\right)^{1.29}\left(\frac{\sqrt{R_{ap}^2 + R_{ag}^2}}{\rho_\Sigma}\right)^{1.589} \tag{16}$$

where E_Σ is equivalent elastic modulus, α_0 is the viscosity coefficient, f_n is the unit normal loading, ρ_Σ is the equivalent curvature radius, R_{ap} and R_{ag} are the roughness of conjugate tooth surface.

The relative sliding distance s can be expressed as follows:

$$s = 2a_H\left(\frac{v_1}{v_2} - 1\right) \tag{17}$$

where a_H is the contact width on the meshing point, and v_1 and v_2 are the relative motion velocity on the meshing point.

The spiroid gear tooth surface can be divided into several contact lines. Taking one contact line as the research object and dividing it into m meshing points, the wear characteristics of the tooth surface can be analyzed by calculating the wear depth in a small area near the meshing point, as shown in Figure 6.

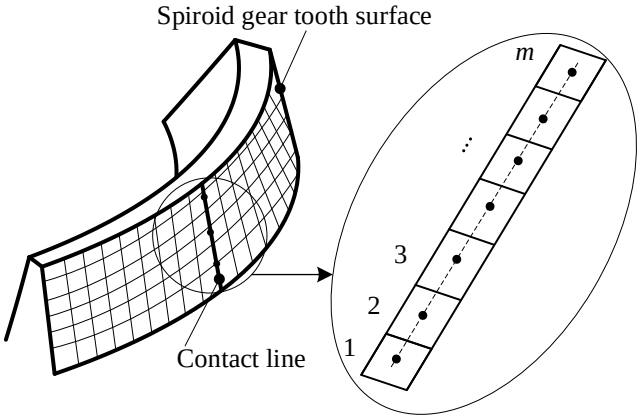

Figure 6. Division of meshing surface and contact line.

Based on the modified Archard model of Equation (15), the wear depth on spiroid worm drive can be indicated as:

$$h = \int_0^s kpds \tag{18}$$

According to the discrete contact points in Figure 6, the total wear depth can be calculated by the limited number of discrete points. The wear depth on the spiroid worm drive tooth surface in the nth meshing cycles can be expressed as:

$$h_n = h_{n-1} + kp_{n-1}s \tag{19}$$

While the spiroid gear surface is worn, its tooth profile will change, which will affect the contact stress and contact half width at the contact point in the next meshing cycle. According to the gear geometry of the spiroid gear tooth surface, the worn tooth profile of the spiroid gear is established, as shown in Figure 7.

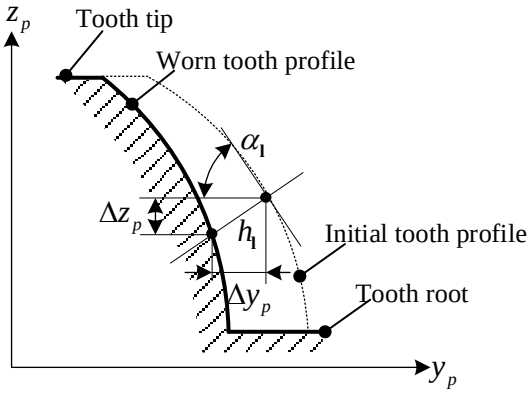

Figure 7. Profile model after wear.

3.3. Numerical Analysis of Wear Performance

Based on the mathematical model of wear performance and the parameters for wear calculation in Table 2, the wear depth of spiroid worm drive can be calculated. The wear depth of each meshing point on the contact line between the left flank and right flank are shown in Figure 8.

Table 2. Parameters for wear calculation.

Parameters	Unit	Value
Output Torque	T_2/N·m	100
Elastic modulus	E/Pa	2.11×10^{11}
Poisson's ratio	u_p	0.28
Wear coefficient	k/m^2 N^{-1}	5×10^{-16}
Worm input speed	n_1/rpm	1500
Total length of left flank contact line	$L_{\sum l}$/mm	50.1
Total length of right flank contact line	$L_{\sum r}$/mm	54.4

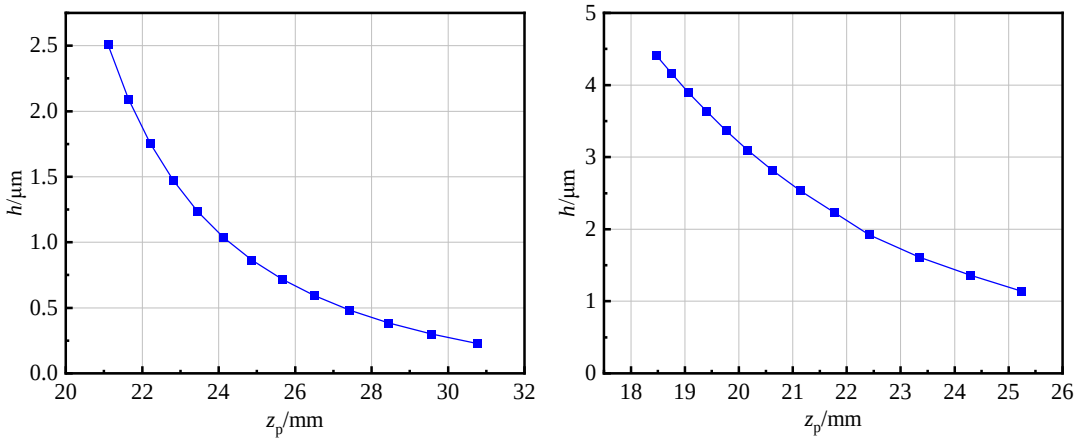

(**a**) Left flank (**b**) Right flank

Figure 8. Wear depth at meshing points on spiroid gear.

The wear depth on both surfaces of the spiroid gear tooth surface are calculated in micrometers. Observing the wear pattern, the depth diminishes progressively from the tooth's apex toward its base along the height. Notably, the region closest to the apex exhibits a higher susceptibility to wear. According to the results of Figures 4 and 5, the lubrication conditions at the tooth tip are relatively poor compared to the tooth root, which is consistent with the variation in wear depth.

Comparing the wear depth of the two spiroid gear tooth surfaces, it is observed that the right flank exhibits a greater degree of wear than the left flank. This finding aligns with the earlier conclusion from Section 2.1, which noted that the left flank benefits from superior overall lubrication compared to the right flank.

Figure 9 illustrates the correlation between wear depth and pressure angle. By plotting the tooth angle on the horizontal axis and the maximum wear depth along the contact line on the vertical axis, the relationship between the pressure angle and the peak wear depth for each tooth profile angle is determined. The results indicate that the maximum wear depth at the meshing point decreases progressively as the pressure angle rises. At the same time, the wear depth near the meshing end is smaller than that at the meshing end, and the wear depth on left flank is smaller than that on right flank.

As depicted in Figure 10, the variation in wear depth with respect to the cone angle is analyzed. The relationship between the cone angle and the maximum wear depth along the contact line is plotted, with the tooth angle on the horizontal axis and the wear depth on the vertical axis. The results reveal that as the cone angle increases, the wear depth at the meshing point gradually diminishes, with lubrication conditions aligning with this trend. During the transition of the worm gear in the spiroid drive from a conical to a cylindrical shape, both lubrication quality and meshing performance experience a slight

decline, accompanied by a marginal increase in wear. Additionally, the left flank exhibits less wear compared to the right flank.

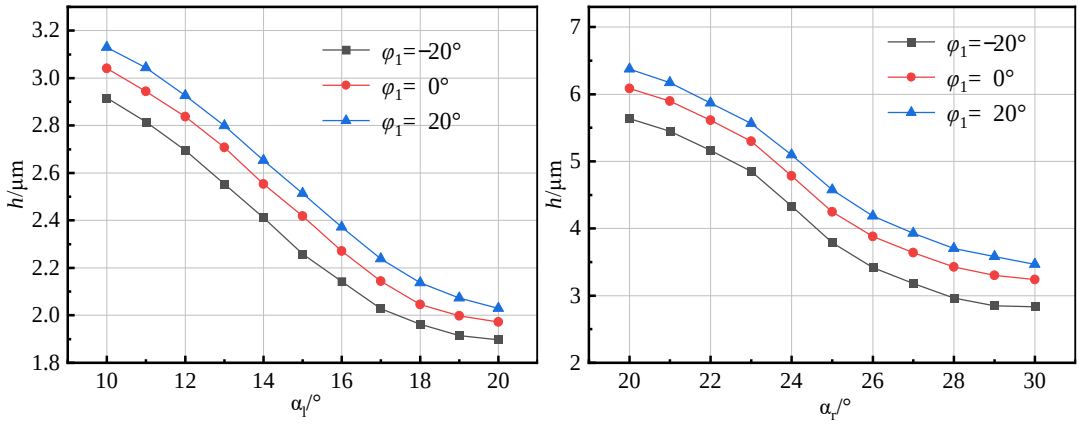

(**a**) Left flank (**b**) Right flank

Figure 9. Wear depth varying with pressure angle.

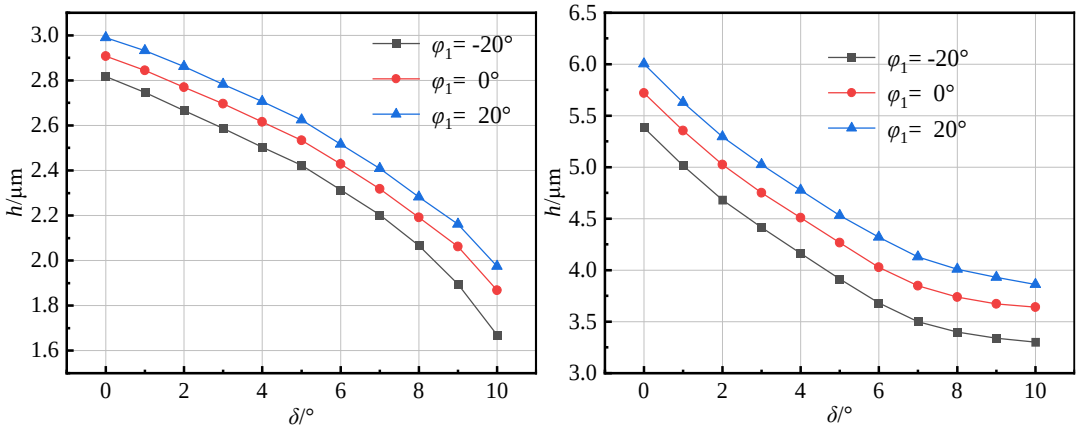

(**a**) Left flank (**b**) Right flank

Figure 10. Wear depth varying with cone angle.

4. Experimental Verification of Wear Performance

4.1. Experimental Principle

To simulate the friction system of steel-to-steel in the spiroid worm drive, the pin disc rotation friction testing is carried out with different lubrication angles and induced normal curvature.

The experimental principle of wear testing is shown in Figure 11. As shown in the schematic diagram, a positive pressure P_n is applied on the pin, with the end face arc radius R according to the k_δ. During the testing, the pin and the disc contact with a line, and the pin is fixed, while the disk rotates at an angular velocity of w, and the included angle θ according to the θ_v.

The geometric relationship of wear area in the pin end face is shown in Figure 12; b is the width of contact area, and the wear depth can be expressed as follows:

$$\begin{aligned} h &= R - \sqrt{R^2 - \frac{b^2}{4}} \\ &= \frac{1}{K_\sigma} - \sqrt{\frac{1}{K_\sigma^2} - \frac{b^2}{4}} \end{aligned} \tag{20}$$

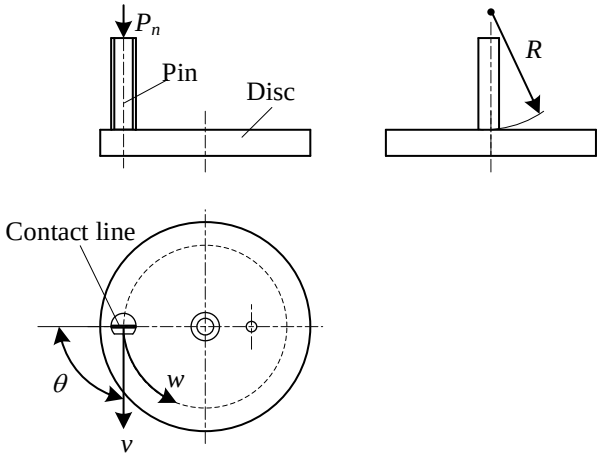

Figure 11. Schematic diagram of wear testing.

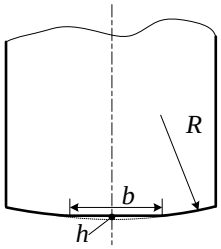

Figure 12. Schematic diagram of wear area.

Based on the testing principle, the MFT-500 highly integrated multifunctional friction and wear testing machine is used to test the wear of spiroid worm tooth surface. The rotating module of wear testing is shown in Figure 13, and the technical parameters of the MFT-500 is shown in Table 3.



Figure 13. Rotating module of wear testing.

Table 3. Key technical parameters of MFT-500.

Parameters	Unit	Value
Maximum load	N	2000
Operating speed of rotating module	rpm	0.1~3000
Operating temperature	°C	20~1000
Maximum travel of X-Y axis	mm	250
Maximum speed of X-Y axis	m/s	10

4.2. Experimental Preparation

According to the k_δ in Figure 4 and the θ_v in Figure 5, the experimental parameters are designed as shown in Table 4.

Table 4. Experimental parameters.

Parameters	Unit	Value
Testing load	N	150
Induced normal curvature	mm^{-1}	0.025/0.029/0.031/0.035
Lubrication angle	°	0/22.5/45/67.5/90
Speed of rotating module	rpm	150
Lubricant oil		460#
Operating temperature	°C	25
Operating time	h	2
Material		42CrMo
Surface hardness	HRC	55~60
Surface roughness	μm	0.8

To meet the induced normal curvatures in Table 2, the end face of the pin is ground through the method shown in Figure 14. A grinding fixture is used to grind the end face of the pin, and pin I and pin II are assembled in the hole based on the reference surface, which is parallel to the axis of the external grinding machine, as well as the pin fixed through the set screw. Through controlling the cylindrical radius R of the two pins end faces, the induced normal curvatures can be precisely ground. Based on the reference surface in the pin, the lubrication angle can be precisely assembled by rotating the pin.

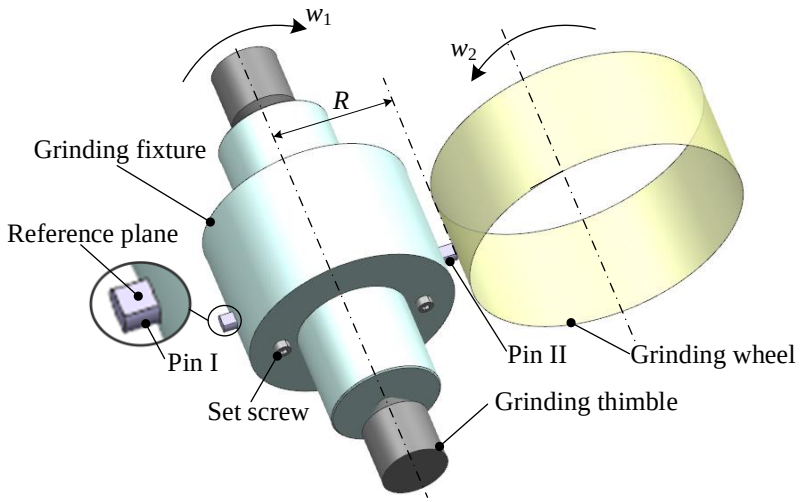

Figure 14. Grinding method of pin end face.

4.3. Experiment and Results

Based on the aforementioned principles and basic parameters, the pin and the disc are manufactured, and the friction and wear testing are carried out. The wear area of the pin end face and the disc are shown in Figure 15.

The width of the contact area on the pin end face is measured by the VHX-1000C/VW-6000 super depth of field 3D microscopic system, as shown in Figure 16.



(**a**) Pin (**b**) Disc

Figure 15. Experimental samples after wear.

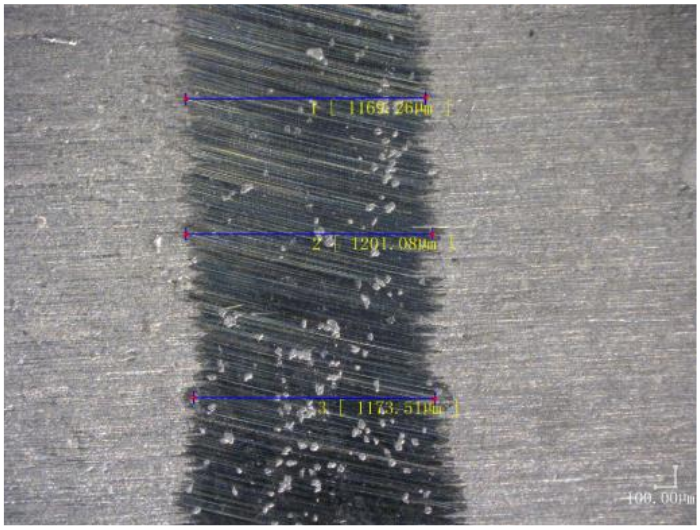

Figure 16. Width of contact area.

The wear depth of the sample pins in each group is shown in Figure 17. It can be known that the wear depth of the sample pins are all below 15 μm. As the lubrication angle increases, the wear depth of the pins gradually decreases under various induced curvature radii. The trend of wear depth reduction is smoother when the lubrication angle is between 45° and 90° than when it is between 0° and 45°. With the same lubrication angle, the wear depth of the pin decreases with the increase of the induced curvature radius, and this trend is most pronounced at a lubrication angle of 0°. When the lubrication angle is large, the wear depth of the pin under different induced curvature radii is relatively close.

These experimental results are consistent with the analysis of wear characteristics in Section 2 and also indicate that when the lubrication angle of the transmission pair teeth is large, the wear degree of each meshing point is closer and the wear depth is smaller, thus reflecting the advantages of a spiroid worm drive and the feasibility of steel-to-steel material meshing.

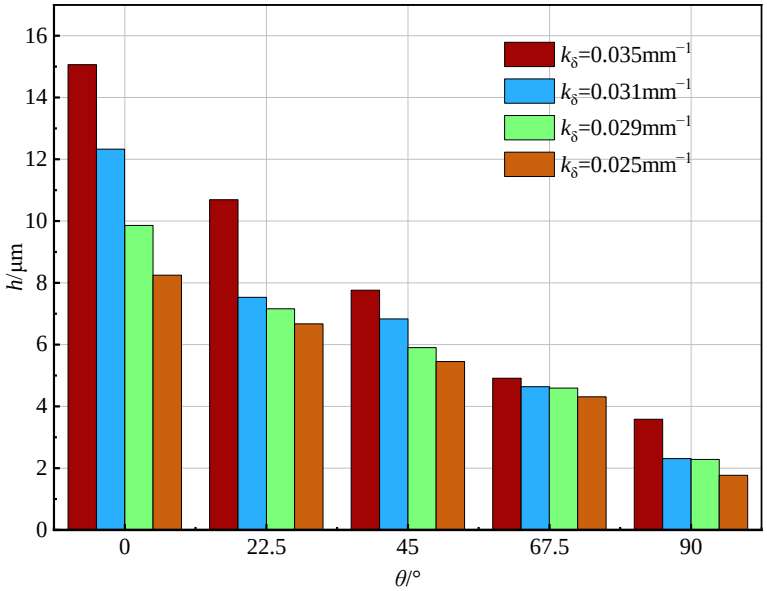

Figure 17. Wear depth of pin end surface.

5. Performance Testing of Spiroid Worm Drive

5.1. Experimental Scheme

The spiroid worm drive is manufactured as shown in Figure 18. The testing gearbox is assembled and the testing platform is shown in Figure 19, while the main parameters of experimental devices are in Table 5.



(**a**) Spiroid worm (**b**) Spiroid gear

Figure 18. Manufacturing of spiroid worm drive.

Table 5. Main parameters of the experimental devices.

No.	Devices	Model	Parameters	Unit	Value
1	Servo motor	ZJY-5.5-1500J	Rated power	kW	5.5
			Rated torque	Nm	35
			Rated speed	rpm	1500
2	Input sensor	HBM-T40B	Torque range	Nm	100
3	Spiroid worm drive	A90-I50	Gear ratio		50
4	Output sensor	HBM-T40B	Torque range	Nm	5000
5	Speed reducer	ZDY160	Gear ratio		4
6	Powder brake	CZ-50	Rated load	Nm	500

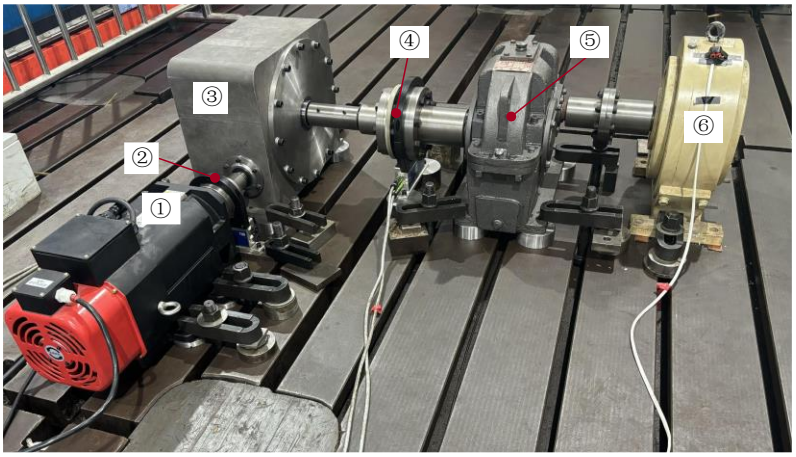

Figure 19. Experimental testing platform. 1—Servo motor, 2—Input sensor, 3—Spiroid worm drive, 4—Output sensor, 5—Speed reducer, 6—Powder brake.

5.2. Performance Testing

At a rated speed of 1500 rpm in the spiroid worm drive, the transmission efficiency initially rises with an increasing load but eventually declines, as illustrated in Figure 20. The red curve represents the transmission efficiency of spiroid worm drive meshing with the left flank, while blue curve represents the transmission efficiency of spiroid worm drive meshing with the right flank. When the transmission efficiency reaches around 70%, the efficiency change amplitude is relatively small during subsequent loading. It can be seen that the transmission efficiency of the left flank reaches its maximum value of about 73.9% at the load of 1100 Nm, while the right flank reaches its maximum value of about 74.3% at the load of 1400 Nm, which is consistent with the theoretical analysis conclusion in Figures 4 and 5. The transmission efficiency is slightly higher than that of traditional steel–bronze meshing worm drive [32].

To verify the wear characteristics analysis of the spiroid worm tooth surface, the following experimental conditions were carried out. The input speed was set as 1500 rpm, while the output load was 1000 Nm, and the prototype was continuously operated for about 3 h for each surface. The wear status of the tooth surface is shown in Figures 21 and 22.

From Figures 19 and 20, it is evident that the wear marks on the spiroid gear tooth surface are more pronounced compared to those on the spiroid worm tooth surface. Additionally, the wear on the right flank of the spiroid worm is notably more severe than on left flank, aligning with the theoretical findings presented in Figure 6.

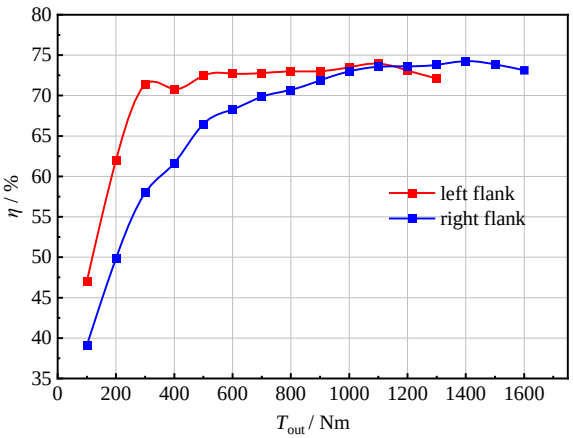

Figure 20. Transmission efficiency of the spiroid worm drive.

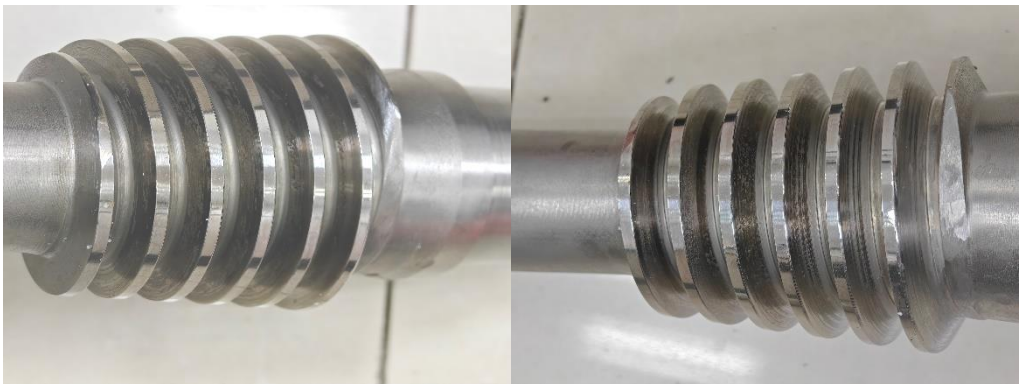

(**a**) Left flank (**b**) Right flank

Figure 21. Wear status on the spiroid worm tooth surface.

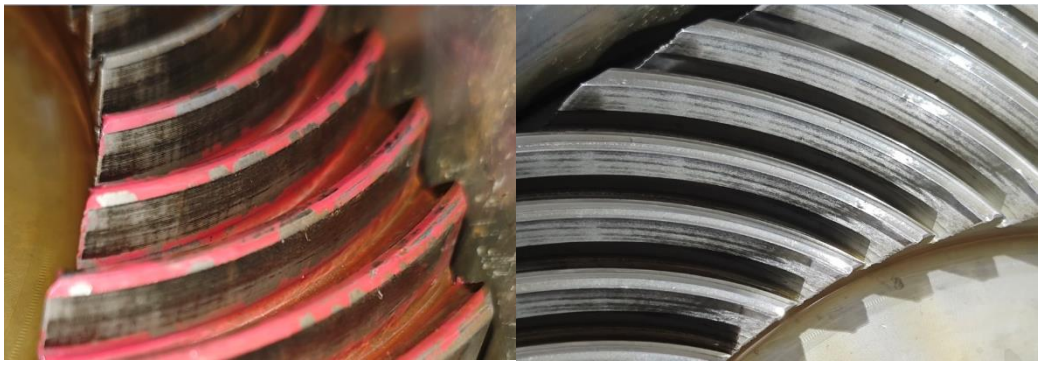

(**a**) Left flank (**b**) Right flank

Figure 22. Wear status on the spiroid gear tooth surface.

At the unloaded flank of the spiroid gear left flank, there is a noticeable area where the wear depth is significantly smaller than other parts of the tooth surface, and the wear depth at the loaded flank is even smaller. For the spiroid gear right flank, the most obvious wear marks are mainly concentrated at the unloaded flank, which proves that the wear at the unloaded flank of the spiroid gear right flank is also smaller than that at the loaded flank.

6. Conclusions

This study mainly analyzes the wear performance of the spiroid worm drive tooth surface through the digital calculation, the pin-disk friction and wear testing, as well as the spiroid worm drive prototype performance testing. From the results provided, we can draw the following conclusions:

(1) The induced normal curvatures are less than 0.04 mm^{-1} and the lubrication angles are greater than 70° on the conjugate tooth surfaces, and there are good lubrication and anti-wear characteristics in the spiroid worm drive.
(2) The wear amount on the right flank is twice that of the left flank, the wear depth on both surfaces gradually decreases along the tooth height direction from the top of the spiroid gear tooth to the root, and the wear depth at the loaded flank is smaller than that at the unloaded flank.
(3) The wear depth of the sample pins is all below 15 μm, and the wear depth of the pins gradually decreases under various induced curvature radii as the lubrication angle increases.
(4) With the same lubrication angle, the wear depth of the pin decreases with the increase of the induced curvature radius, and this trend is most pronounced at a lubrication

angle of 0°. When the lubrication angle is large, the wear depth of the pin under different induced curvature radii is relatively close.

(5) The feasibility of steel–steel meshing in spiroid worm drive has been confirmed, and the transmission efficiency of the left flank is about 73.9% at the load of 1100 Nm, while the right flank is about 74.3% at the load of 1400 Nm.

Author Contributions: Conceptualization, Y.C. (Yan Chen) and Y.C. (Yonghong Chen); methodology, Y.C. (Yonghong Chen); validation, Y.C. (Yan Chen) and Y.P.; investigation, Y.C. (Yan Chen); resources, Y.C. (Yonghong Chen); data curation, Y.C. (Yan Chen); writing—original draft preparation, Y.C. (Yan Chen) and Y.C. (Yonghong Chen); writing—review and editing, Y.C. (Yonghong Chen); project administration, Y.P.; funding acquisition, Y.C. (Yonghong Chen). All authors have read and agreed to the published version of the manuscript.

Funding: This research was funded by the National Natural Science Foundation of China (52075054).

Data Availability Statement: Data are reported within the article.

Conflicts of Interest: The authors declare no conflicts of interest.

Nomenclature

Symbols	Definition	Unit
A	Center distance	mm
E_{Σ}	Equivalent elastic modulus	Pa
f_{n}	Unit normal loading	N
F_{n}	Normal load	N
h	Wear depth	mm
H	Material hardness	/
h_a	Full tooth height of spiroid worm	mm
h_w	Working tooth height of spiroid worm	mm
i_{12}	Transmission ratio	/
k	Wear coefficient	/
k_δ	Induced normal curvature	mm^{-1}
L_w	Length of worm thread	mm
m_δ	Modulu along generatrix of spiroid worm	mm
n_1	Input speed of spiroid worm	rpm
p	Contact pressure at the meshing point	N
p_{t}	Radial helix parameter	/
q	Diameter coefficient for spiroid worm	/
R_{ap}	Roughness of spiroid worm	μm
R_{ag}	Roughness of spiroid gear	μm
s	Relative sliding distance	mm
S_{s}	Coordinate systems rigidly attached to spiroid worm	/
S_{t}	Coordinate systems rigidly attached to turning tool	/
S_{m}	Fixed coordinate systems with spiroid worm	/
S_{n}	Fixed coordinate systems with spiroid gear	/
S_{P}	Coordinate systems rigidly attached to spiroid gear	/
T_2	Output torque of spiroid gear	Nm
u	Surface parameter	/
u_{p}	Poisson's ratio	/
V	Wear volume	mm^3
v_1	Relative motion velocity of spiroid worm	m/s
v_2	Relative motion velocity of spiroid gear	m/s
ω_1	Angular velocity of spiroid worm	rad^{-1}
ω_2	Angular velocity of spiroid gear	rad^{-1}

Z_A	Offset distance	mm
Z_1	Number of spiroid worm threads	/
α_0	Viscosity coefficient	/
α_l	Pressure angle on left flank	°
α_r	Pressure angle on right flank	°
a_H	Contact width on meshing point	mm
δ	Cone angle	°
δ_{a2}	Half cone angle of spiroid worm	°
θ_v	Lubrication angle	°
ρ_Σ	Equivalent curvature radius	mm
φ_1	Instantaneous rotation angles of spiroid worm	rad
φ_2	Instantaneous rotation angles of spiroid gear	rad
φ_u	Rotating angle of turning tool	rad

References

1. Chen, Y.; Chen, Y.; Luo, W.; Zhang, G. Development and classification of worm drive. In Proceedings of the 14th IFToMM World Congress, Taiwan, China, 25–30 October 2015.
2. Goldfarb, V. What we know about spiroid gears. In Proceedings of the International Conference on Mechanical Transmissions, Chongqing, China, 26–30 September 2006.
3. Goldfarb, V.; Trubachev, E.; Kuznetsov, A.; Makarov, V. Development and manufacturing of spiroid gear drives for pipeline valves. In Proceedings of the International Conference on Mechanical Transmissions, Chongqing, China, 26–30 September 2006.
4. Goldfarb, V.; Trubachev, E.; Barmina, N. Innovations in design and production of spiroid gears in the XXI century. In Proceedings of the 6th International BAPT Conference on Power Transmissions, Varna, Bulgaria, 19–22 June 2019.
5. Litvin, F.; Argentier, G.; Donno, M.; Hawkins, M. Computerized design, generation and simulation of meshing and contact of face worm-gear drives. *Comput. Methods Appl. Mech. Eng.* **2000**, *189*, 785–804. [CrossRef]
6. Litvin, F.; Fuentes, A.; Gonzalez, I.; Carvenali, L.; Kawasaki, K.; Handschuh, R. Modified involute helical gears: Computerized design, simulation of meshing and stress analysis. *Comput. Methods Appl. Mech. Eng.* **2003**, *192*, 3619–3655. [CrossRef]
7. Fuentes, A.; Gonzalez, I. Mathematical definition and computerized modeling of spherical involute and octoidal bevel gears generated by crown gear. *Mech. Mach. Theory* **2016**, *106*, 94–114. [CrossRef]
8. Temirkhan, M.; Spitas, C.; Wei, D. A computationally robust solution to the contact problem of two rotating gear surfaces in space. *Meccanica* **2023**, *58*, 2455–2466. [CrossRef]
9. Bodzas, S.; Dudas, I. Mathematical description and modeling of a tooth surface of spiroid face gear having arched profile in axial section. *Int. J. Adv. Manuf. Technol.* **2016**, *84*, 1431–1442. [CrossRef]
10. Balajti, Z. Determination of undercutting avoidance for designing the production technology of worm gear drives with a curved profile. *Machines* **2023**, *11*, 56. [CrossRef]
11. Zhao, Y.; Kong, X. Meshing principle of conical surface enveloping spiroid drive. *Mech. Mach. Theory* **2018**, *123*, 1–26. [CrossRef]
12. Huai, C.; Zhao, Y. Influence of grinding wheel parameters on the meshing performance of toroidal surface enveloping conical worm drive. *Mech. Sci.* **2019**, *10*, 199–211. [CrossRef]
13. Zhao, Y.; Meng, Q. Curvature interference characteristic of conical surface enveloping conical worm. *Forsch. Ingenieurwesen* **2017**, *81*, 409–419. [CrossRef]
14. Mu, S.; Zhao, Y.; Cui, J.; Meng, Q.; Li, G. Meshing limit line of face worm gear drive with hardened cylindrical worm. *Proc. Inst. Mech. Eng. Part C-J. Mech. Eng. Sci.* **2022**, *236*, 9882–9899. [CrossRef]
15. Mu, S.; Zhao, Y.; Cui, J.; Meng, Q.; Li, G. Meshing theory of face worm gear drive with hardened cylindrical worm. *Mech. Mach. Theory* **2023**, *185*, 105323. [CrossRef]
16. Xu, Z.; Li, H.; Ren, W.; Ma, M. Investigation of non-linear dynamic characteristics of a point-contact spiroid worm drive generated by two-generating-surface method. *J. Sound Vib.* **2025**, *597*, 118805. [CrossRef]
17. Xian, W.; Chen, Y.; Gao, J.; Luo, W.; Chen, B. Meshing performance investigations on face worm gear drive with the variable worm cone angle. *J. Adv. Mech. Des. Syst. Manuf.* **2023**, *17*, 2300273. [CrossRef]
18. Staniek, R. Positioning accuracy investigations in face spiroid gears. In Proceedings of the 8th Biennial Conference on Engineering Systems Design and Analysis, Torino, Italy, 4–7 July 2006.
19. Gessner, A.; Staniek, R. Backlash adjustment in plane spiroid gears. In Proceedings of the 8th Biennial Conference on Engineering Systems Design and Analysis, Torino, Italy, 4–7 July 2006.
20. Evgeniy, S.; Kirill, V.; Tatyana, A. Advanced method of cutting spiroid, worm and bevel gearwheel teeth by running-in cutter heads. *Forsch. Ingenieurwesen* **2022**, *86*, 709–719.

21. Li, Y.; Yang, J.; Gu, R.; Chen, Z.; Xia, C. Mathematical modeling and generating method of hourglass worm gear hob's rake face based on a rotating paraboloid surface. *Machines* **2024**, *12*, 770. [CrossRef]
22. Balajti, Z.; Mandy, Z. Proposed solution to eliminate pitch fluctuation in case of conical screw surface machining by apex adjustment. In Proceedings of the 30th International Conference on Flexible Automation and Intelligent Manufacturing, Athens, Greece, 7–10 September 2021.
23. Tkachuk, A.; Ignatyugin, V. Grinding the side surfaces of the spiroid cylindrical gear worm turns with a tapered wheel. In Proceedings of the 2023 International Scientific Siberian Transport Forum, Novosibirsk, Russia, 16–19 May 2023.
24. Chodola, L.; Mazurkow, A.; Surowaniec, M.; Markowski, T.; Homik, W. Measurement method of temperature of the face gear rim of a spiroid gear. *Sensors* **2022**, *22*, 8860. [CrossRef]
25. Tošić, M.; Larsson, R.; Stahl, K.; Lohner, T. Thermal elastohydrodynamic analysis of a worm gear. *Machines* **2023**, *11*, 89. [CrossRef]
26. Mazurkow, A.; Homik, W. Operation of a spiroid gear under elastohydrodynamic luberication conditions. *Transp. Probl.* **2024**, *19*, 141–153.
27. Zaitsev, A. Estimation of the resource of spiroid transmissions by the condition maximum wear and tear. In Proceedings of the International School on Neural Networks, St. Petersburg, Russia, 8–10 February 2022.
28. Zengeya, P.; Mao, K.; Goodship, V. The effects of cooling rate (mould temperature) on HDPE gears produced through injection moulding. *Wear* **2023**, *530*, 205000. [CrossRef]
29. Skulić, A.; Bukvic, M.; Gajevic, S.; Miladinovic, S.; Stojanovic, B. The influence of worm gear material and lubricant on the efficiency and coefficient of friction. *Tribol. Mater.* **2024**, *3*, 15–23. [CrossRef]
30. Litvin, F.; Fuentes, A. *Gear Geometry and Applied Theory*, 2nd ed.; Cambridge University Press: New York, NY, USA, 2004; pp. 547–613.
31. Huangfu, Y.; Dong, X.; Cao, Y.; Li, Y.; Peng, Z.; Sun, Y. Life-cycle dynamic wear degradation model of planetary gear systems. *Wear* **2024**, *542*, 205281. [CrossRef]
32. Skulic, A.; Milojevic, S.; Maric, D.; Ivanovic, L.; Krstic, B.; Radojkovic, M.; Stojanovic, B. The impact of lubricant viscosity and materials on power losses and efficiency of worm gearbox. *Teh. Vjesn.* **2022**, *29*, 1853–1860.

Disclaimer/Publisher's Note: The statements, opinions and data contained in all publications are solely those of the individual author(s) and contributor(s) and not of MDPI and/or the editor(s). MDPI and/or the editor(s) disclaim responsibility for any injury to people or property resulting from any ideas, methods, instructions or products referred to in the content.